

Improved performance of polarization-stable VCSELs by monolithic sub-wavelength gratings produced by soft nano-imprint lithography

M A Verschuuren¹, P Gerlach², H A van Sprang¹ and A Polman³

¹ Philips Research, High Tech Campus 4, 5656 AE Eindhoven, The Netherlands

² Philips Technologie GmbH U-L-M Photonics, Albert-Einstein-Allee 45, 89081 Ulm, Germany

³ Center for Nanophotonics, FOM Institute AMOLF, Science Park 104, 1098 XG Amsterdam, The Netherlands

Received 25 July 2011, in final form 4 October 2011

Published 23 November 2011

Online at stacks.iop.org/Nano/22/505201

Abstract

We present a novel method for fabricating polarization-stable oxide-confined single-mode GaAs based vertical cavity surface emitting lasers (VCSELs) emitting at 850 nm using a new soft-lithography nano-imprint technique. A monolithic surface grating is etched in the output mirror of the laser cavity using a directly imprinted silica-based sol-gel imprint resist as an etch mask. The opto-electronic performance of these devices is compared to VCSELs fabricated by state-of-the-art electron-beam lithography. The lasers made using the soft nano-imprint technique show single-mode TM lasing at a threshold and laser slope similar to that of devices made by e-beam lithography. The soft nano-imprint technique also enables the fabrication of gratings with sub-wavelength pitch, which avoids diffraction losses in the laser cavity. The resulting single-mode VCSEL devices exhibit 29% enhanced efficiency compared to devices equipped with diffractive gratings.

(Some figures may appear in colour only in the online journal)

1. Introduction

Single-mode vertical cavity surface emitting lasers (VCSELs) find application in tunable diode laser absorption spectroscopy [1, 2], laser based optical mouse sensors, optical encoders and rubidium atomic clocks for GPS systems [3, 4]. These applications require single-mode and single-polarization emission. Due to the symmetry of a VCSEL device the laser does not have a geometrically defined single-polarization orientation [5–10]. Emission occurs along both the $\langle 100 \rangle$ and $\langle 010 \rangle$ GaAs crystal planes. As a result the polarization can spontaneously switch between these two directions during operation of the laser, which is not desired.

One method to avoid the switching of the polarization mode during laser operation is to apply a monolithic surface grating to one of the dielectric distributed Bragg reflector (DBR) mirrors of the VCSEL laser cavity [11, 12]. A grating exhibits different reflection coefficients for TE and

TM polarized light. The polarization mode with the higher reflectivity and thus the higher cavity quality factor will have the lowest threshold pump current for gain. As a result the polarization with the highest reflectivity will become the dominant lasing mode. Currently, polarization-locked VCSELs use gratings made by standard electron-beam lithography [13]. Grating pitches are typically as large as 550 nm, as smaller pitches would increase the e-beam writing time and thus costs. This large pitch causes diffraction of a significant fraction of light, and as a result the efficiency of stabilized VCSELs is reduced. Depending on the laser design and mirror reflectivity, the efficiency loss can be up to 50% [14].

Chu *et al* proposed the use of sub-wavelength transmission gratings, that do not exhibit high-order diffraction, in an external cavity design to stabilize the VCSEL polarization [15]. As this is not a monolithic integrated solution, cavity length and temperature are more difficult to control and laser

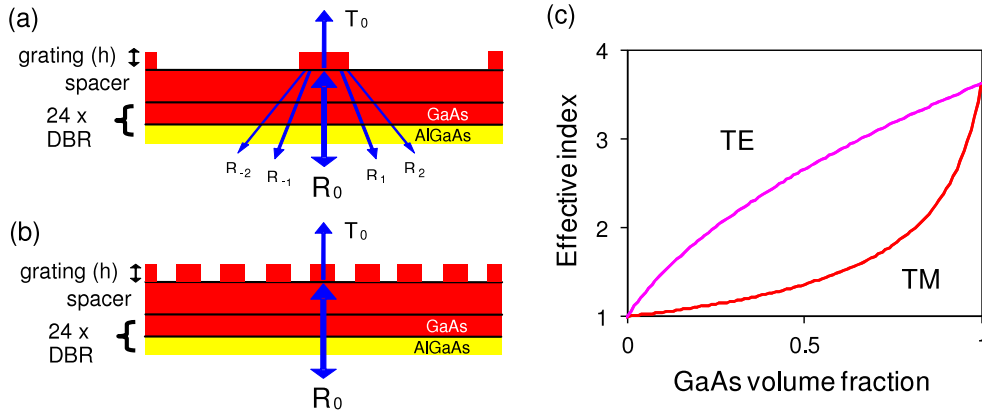


Figure 1. (a), (b) Schematic of top (output) DBR cavity laser mirror with integrated grating. (a) 550 nm-pitch grating, the arrows indicate diffraction into higher-order grating modes. (b) 150 nm-pitch grating, which exhibits only zeroth order reflection. (c) Effective refractive index for TE and TM polarizations, calculated using an effective medium approximation, for perpendicular incidence on gratings in GaAs as function of the GaAs volume fraction.

operation is less stable. Gustavsson *et al* used electron-beam lithography to pattern sub-wavelength gratings in an integrated approach [16]. However, this solution requires a very well aligned localized grating on the output mirror which is difficult to produce. Moreover this method is not well suited for mass production. Here, we demonstrate polarization-stabilized VCSELs using monolithic surface gratings with a period below the diffraction limit and measure polarization-stable lasing with improved efficiency. To pattern the gratings a novel soft nano-imprint technique is used which enables application over large areas at low cost.

Soft-imprint techniques use a rubber stamp which offers advantages with respect to rigid stamp methods as the soft stamp can conform to substrate bow and surface defects. Also, full wafers can be imprinted without damage to the stamp or substrate. Release of the stamp from an imprinted pattern does not involve high forces as the stamp can be removed by a peeling action; contrary to rigid stamps which require substantial force to initiate release. Previously, soft stamp imprint methods could not reproduce patterns below 100 nm with high fidelity due to deformations of the rubber features. These imprint methods also yielded pattern distortion on a wafer scale, which hampers overlay alignment during subsequent production processes [17–19].

Here, we use a new substrate-conformal imprint lithography (SCIL) technique which offers wafer-scale replication with sub-50 nm resolution and minimal pattern deformations on wafer scales at high throughput. It also enables room-temperature patterning of sol-gel materials which results in stable silicon oxide patterns which can be directly used as a hard mask [20]. This mask is then used to realize monolithic grating structures on VCSEL surfaces.

2. Sub-wavelength grating modeling and design

In this work we study GaAs/AlGaAs VCSELs that operate at 850 nm. The grating is made in GaAs (refractive index $n = 3.63$) and is integrated with the VCSEL DBR mirror (see figures 1(a) and (b)). The maximum grating pitch at

which no higher-order diffraction occurs at $\lambda = 850$ nm in the GaAs grating is given by $d = \lambda/n = 234$ nm. Thus for grating pitches smaller than 234 nm no diffraction will occur at the GaAs-grating and grating-air interface, which would benefit laser performance. The effective refractive index of a grating layer for the two polarization orientations can be estimated with an effective medium approximation using $\varepsilon_{\perp} = (\varepsilon_1 \varepsilon_2) / (f \varepsilon_1 + (1 - f) \varepsilon_2)$ and $\varepsilon_{\parallel} = f \varepsilon_2 + (1 - f) \varepsilon_1$, where $\varepsilon_1 = 1$ and $\varepsilon_2 = 13.81$ are the dielectric constants for air and GaAs, respectively [15, 21]. Figure 1(c) shows the effective refractive index for TE and TM polarizations, calculated for perpendicular incidence on a grating in GaAs as a function of GaAs volume fraction. A large difference in effective index is found for the two polarizations, which will result in a large variation in the reflectivity of the DBR, as we calculate in the next paragraph.

The reflectivity, transmission and diffraction of a DBR mirror with an integrated grating were calculated as function of grating pitch, height and fill fraction. We used the GSolver RCW software package, which uses rigorous coupled wave analysis to calculate the diffraction efficiency of a grating [22]. The reflectivity of the top DBR mirror towards the cavity side was simulated for light incident from the GaAs side. The top DBR mirror consists of 24 pairs of layers of 60 nm-thick AlGaAs ($n = 3.13$) and 65 nm-thick GaAs ($n = 3.63$), covered with a $\lambda/4$ spacer layer of 120 nm GaAs, which isolates the grating layer from the DBR, as schematically indicated in figures 1(a) and (b). In this configuration the GaAs grating layer with varying pitch, height and fill fraction acts as an effective index layer on the $\lambda/4$ spacer layer which can be used to modulate the reflection of the DBR. We simulated two grating pitches: 550 nm which has diffraction orders in reflection at the GaAs interface but not at the air interface, (see figure 1(a)) and a 150 nm grating pitch, which does exhibit diffraction (see figure 1(b)). In the simulation it is assumed there is no absorption in the materials. In figures 2(a) and (b) the zeroth order reflectivity of 850 nm light for polarization orthogonal (TE) and perpendicular (TM) to the grating are plotted as function of grating layer thickness and fill fraction

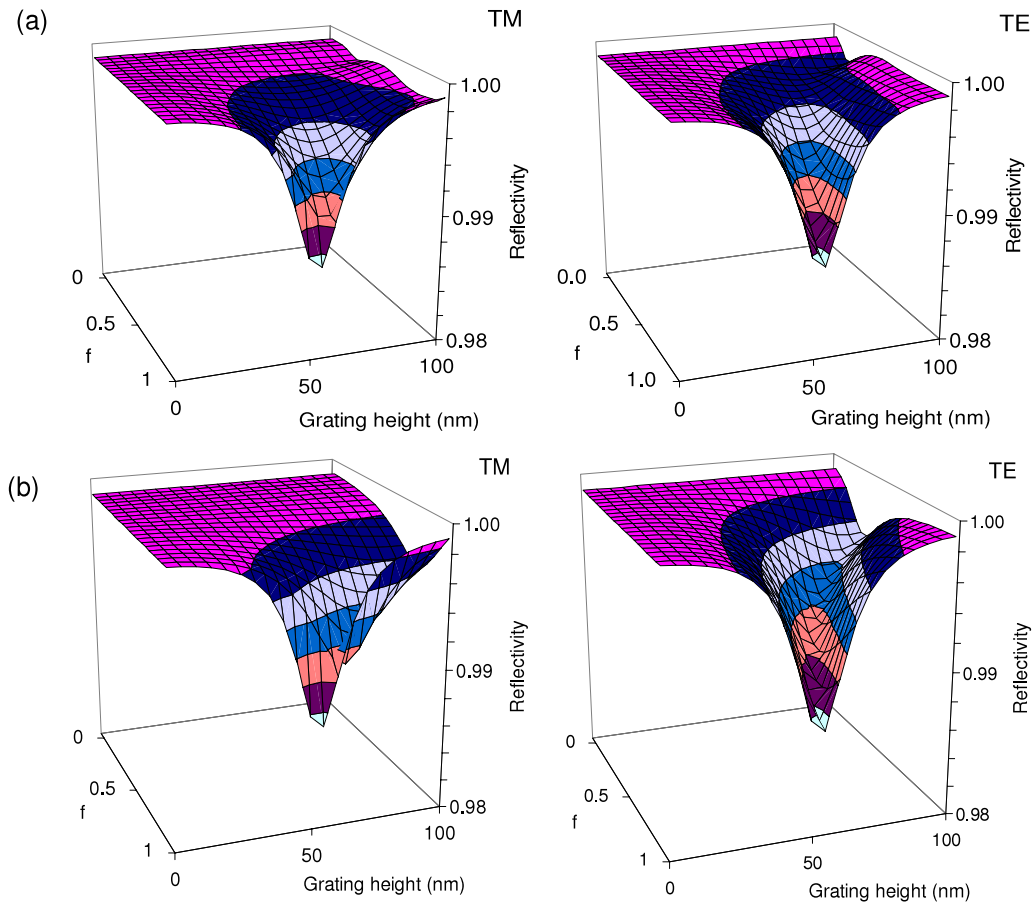


Figure 2. Calculated reflectivity for TM and TE polarized light for a 24-pair BDR with integrated grating as function of grating fill fraction (f) and grating height at $\lambda = 850$ nm: (a) 550-nm pitch grating, (b) 150-nm pitch grating.

for the 550 nm and 150 nm pitch gratings, respectively. In figure 3(a) the difference between TM and TE reflectivity is plotted for 550- and 150-nm pitch gratings. Figure 3(b) plots the fraction of light that is diffracted in higher-order modes for 550 nm gratings as function of grating height and fill fraction.

In theory any difference in TE and TM reflection will result in polarization stabilization. In practice a minimum reflectivity is required for lasing; for polarization locking under all driving conditions the difference in TE and TM reflectivity must then be maximized. Figures 2(a) and (b) show that the 24-pair DBR with only the 120 nm thick GaAs spacer layer (data for grating height = 0) has a reflectivity of 99.90%. Adding the grating layer and taking $f = 1$, leads to a minimum reflectivity of 98.70% for both polarizations for a GaAs top layer thickness of 55 nm. At this thickness, the total GaAs layer on the DBR (see figure 2(a)), corresponds to an optical thickness of one wavelength. Tuning the thickness and fill fraction of the grating layer will thus give a maximum modulation in DBR reflectivity of 1.2%. Figure 3(a) shows that for both grating pitches the TM–TE reflectivity contrast first increases with increasing thickness and then decreases. For a grating height up to 60 nm the TM mode has the highest reflectivity; for large fill fraction and grating layer thickness over 60 nm, the TE mode has the highest reflectivity.

It can also be seen that the reflectivity contrast is largest for the 150-nm pitch grating. In figure 3(b) the sum of

the reflectivity of higher-order grating reflections for the TM mode is plotted as function of grating height and fill fraction for a 550 nm pitch grating. These diffraction losses first increase and then decrease with increasing grating height and fill fraction. The increase is due to an increased scatter cross section, the decrease is due to the higher reflectivity of the DBR/grating combination for increased thickness (see figure 2(a)). Figure 3(b) indicates that to minimize diffraction these gratings have to have limited height and fill fraction.

The reflectivity of the top mirror is mainly determined by the number of DBR pairs. Optimizing the DBR/grating mirror for a polarization-controlled laser requires on the one hand maximum contrast between the reflectivity for TM and TE polarization (figure 3(a)), and on the other hand sufficiently high absolute reflection to obtain a high cavity Q . Here we choose a 550-nm pitch grating design with a thickness of 50 nm and fill fraction of 0.3 which results in a reflectivity of 99.83% with a TM–TE contrast of 7×10^{-4} . This reflectivity is sufficient to obtain acceptable laser threshold and the contrast is sufficient to stabilize the TM mode. For this configuration the diffraction losses are 2.8×10^{-4} (figure 3(b)). This fraction appears relatively low but these losses occur at each optical round trip and correspond to 24.8% of the out-coupled laser intensity.

To compare the performance of 150-nm pitch gratings to diffractive 550-nm pitch gratings we compare structures with

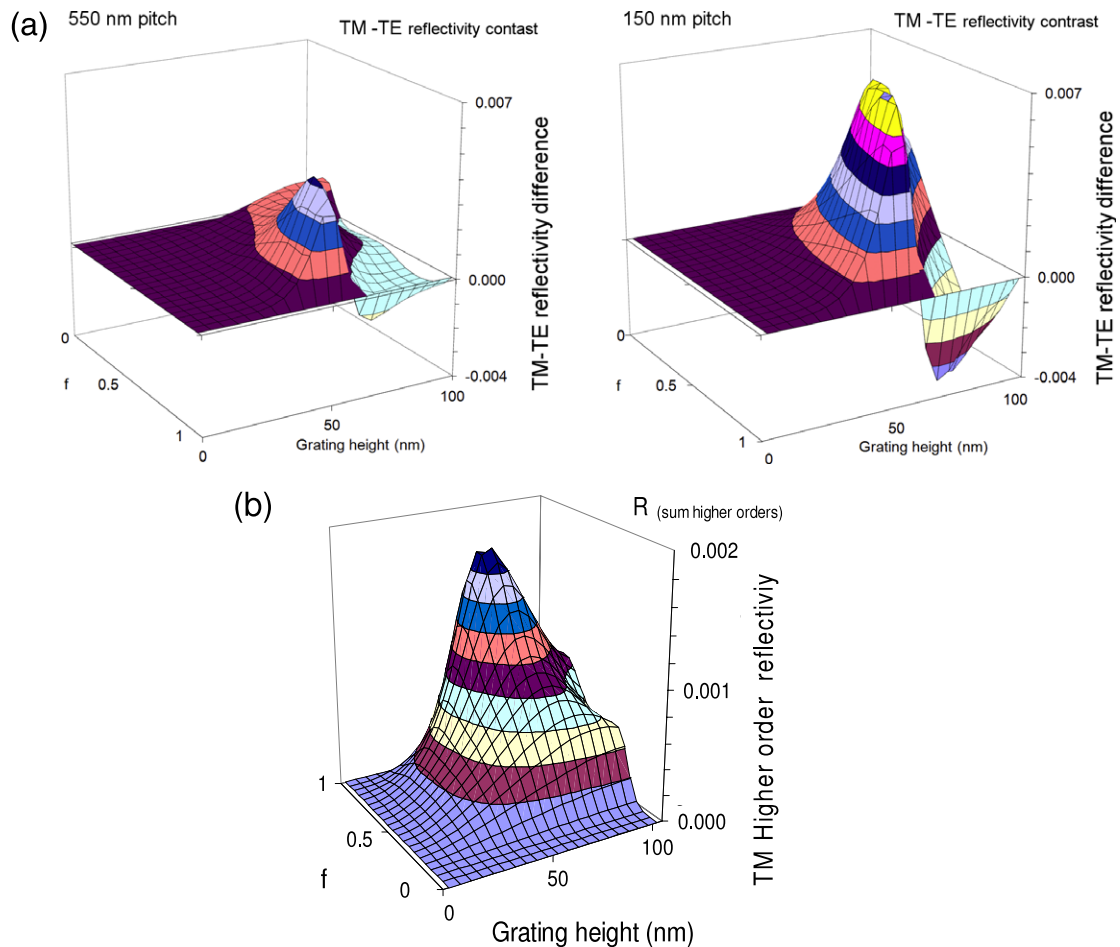


Figure 3. (a) Difference between TM and TE reflectivity at $\lambda = 850$ nm as a function of grating fill fraction (f) and depth for 550-nm pitch and 150-nm pitch gratings on a 24-pair DBR. (b) Fraction of TM polarized light reflected in higher grating orders as a function of grating fill fraction (f) and depth for 550-nm pitch gratings on a 24-pair DBR.

equal absolute TM reflectivity of 99.83%. This reflectivity is obtained for a 150-nm pitch grating with a height of 50 nm and a fill fraction $f = 0.55$ (figure 2(b)). Using this sub-wavelength design we expect a reduced laser threshold as no light is lost in higher-order diffraction modes, which leads to an increased cavity Q . The polarization suppression is also expected to increase, as the reflection contrast is increased to 2.5×10^{-3} , compared to 7.0×10^{-4} in the 550-nm pitch design (figure 3(a)).

Next, we will describe the fabrication of 150- and 550-nm pitch gratings by soft nano-imprint lithography and direct electron-beam patterning. The performance of the electrically driven VCSELs will be compared for both designs and fabrication methods.

3. Fabrication of soft-nano-imprinted VCSELs

3.1. Fabrication of soft-imprint stamps

The two master grating patterns were prepared on 150-mm diameter silicon wafers using a JEOL 100-kV e-beam pattern generator to pattern ZEPP 520 poly(methyl methacrylate) (PMMA) based positive tone electron-beam resist. From these

masters two poly-di-methyl-siloxane (PDMS) stamps were molded which were subsequently used to replicate grating patterns in sol-gel resist.

The ZEPP resist thickness was 100 nm for the 550-nm pitch grating with 165-nm wide lines (grating fill fraction $f = 0.3$) and a thickness of 50 nm for the 150-nm pitch grating with 83-nm wide lines (grating fill fraction $f = 0.55$). The gratings are written over a 3''-diameter area, in 15 μm -diameter circles, placed in a 2D array of 200 μm pitch. Alignment markers were also defined within the 3'' area to align subsequent layers to the grating areas during VCSEL processing. Figure 4(a) schematically shows the layout of the 150-mm diameter master (I) and VCSEL grating area (II) in top and cross section. After development of the resist the surface was modified to ease release of the PDMS stamp. This was done by applying 1,1,2,2-*H*-perfluoro-decyl-tri-chloro-silane by vapor phase deposition for 24 h [23]. The PDMS stamps were directly molded from the fluor-modified e-beam resist, schematically shown in figure 4(a) (III).

The grating patterns on the silicon wafer are molded in PDMS that has a Young's modulus that is higher than that of conventional rubbers, as described in [24]. After mixing and de-gassing the components, a H-PDMS layer 50–100 μm thick

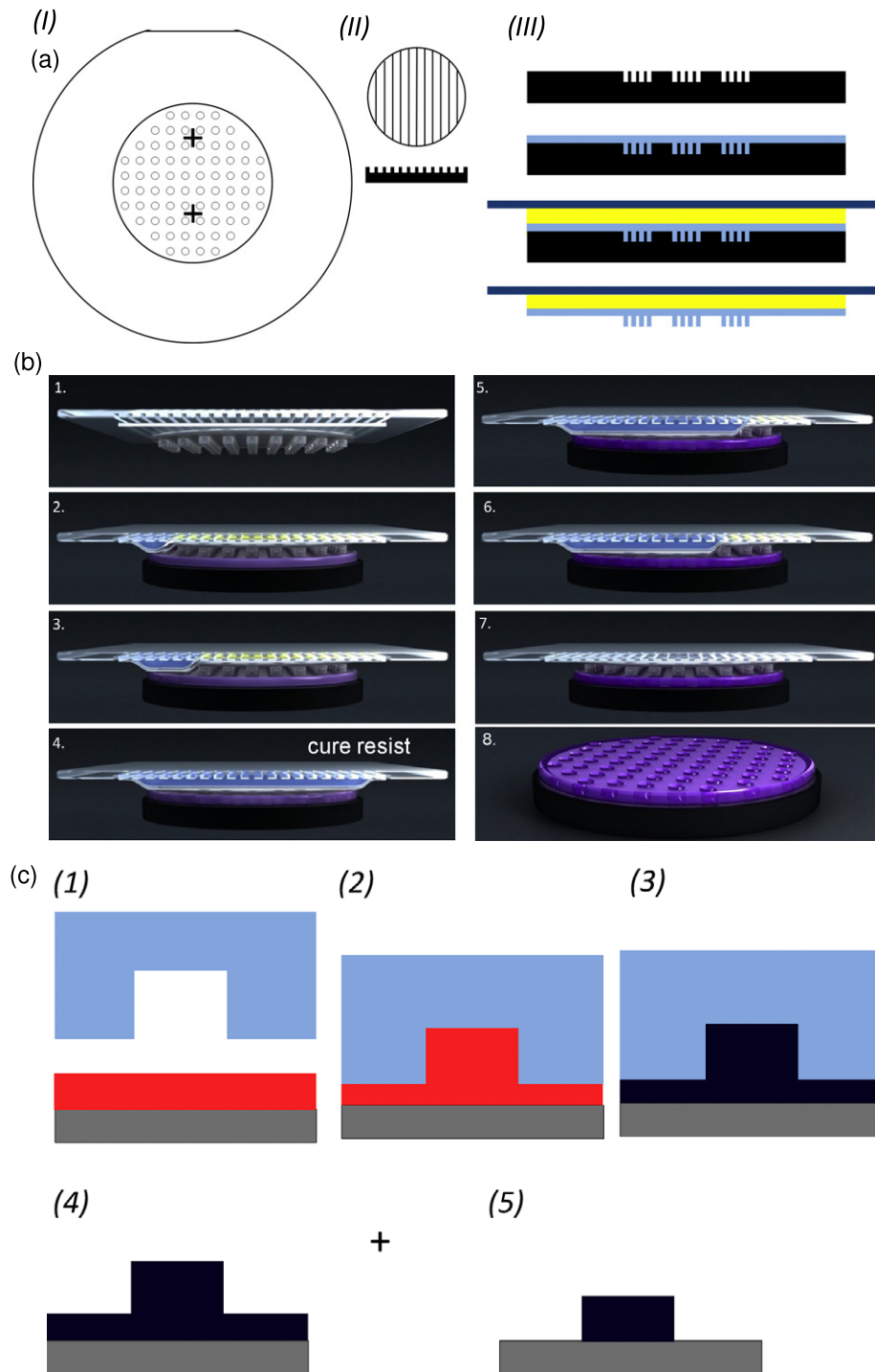


Figure 4. (a)(I) The masters consist of 150 mm wafers that have the VCSEL grating areas patterned in $15\ \mu\text{m}$ circular areas (a)(II) which populate the $3''$ area in a square lattice of pitch $200\ \mu\text{m}$. On two positions alignment markers are defined on the $3''$ area. (a)(III) Composite stamp fabrication by spin coating H-PDMS over the fluor-modified master. This layer is bonded to $200\ \mu\text{m}$ thick glass using low modulus PDMS while the whole stack is co-cured before the stamp is released from the master. (b) Time sequence of an imprint step showing the evolution of the contact area by sequentially pressurizing the grooves. (c) Evolution of the imprint process and break-through etch: (1) continuous sol-gel layer on the VCSEL wafer, (2) application of stamp, recesses are filled by capillary forces, (3) solidification by the formed inorganic network, (4) stamp released, (5) a fluorine base reactive ion etch removes the sol-gel residual layer.

is formed over the masters by spin coating for 30 s at 1000 rpm. After a pre-cure for 15 min at 50°C a defined amount of soft PDMS (Sylgard 184) is poured onto the master. This PDMS is squeezed between the master and a $200\ \mu\text{m}$ thick AF45 glass sheet to form a uniform layer of thickness $\sim 0.5\ \text{mm}$. The

'master-PDMS-glass' sandwich is cured for 24 h in an oven at 50°C . The stamp is released from the master by gentle peeling. Multiple stamps can be molded from the master.

Using this composite soft stamp, pattern deformations are avoided, because during stamp preparation the rubber is

always attached to a carrier, either the master or the glass sheet, which both have high in-plane stiffness. As the glass support is thin, the composite stamp is flexible in the out of plane direction, which allows for substrate non-flatness. The rubber also allows local deformation around particle contaminants, thereby avoiding damage to stamp or substrate.

3.2. Wafer-scale grating replication of VCSEL structures

Wafer-scale imprints are made with SCIL using a flat plate with 80 vacuum grooves, which hold the composite stamp in place. The time sequence of the SCIL imprint process is shown in figure 4(b). A resist coated substrate is placed parallel to the stamp with a spacing of $\sim 100\ \mu\text{m}$. Starting from one side the evacuated grooves are pressurized to an overpressure of ~ 20 mbar. This results in the stamp being gently curved, to bridge the $100\ \mu\text{m}$ gap, after which it forms a line contact on the substrate. As more grooves are sequentially pressurized, capillary forces pull the stamp into the resist and the line contact moves forward which avoids the formation of air inclusions. The stamp is kept in contact until the resist is hardened. Next, the grooves are sequentially evacuated which results in a controlled release of the stamp from the imprinted patterns. With this method, replicated patterns exhibit merely sub-nm deformation over large areas, as demonstrated in [20].

The following imprint process was used to replicate both grating designs (figure 4(c)(1–4)). A silica-based sol–gel was used as the imprint resist, the preparation of which is described in [20]. The sol–gel resist was applied by spin coating on the as-grown VCSEL layer stack on 3" GaAs wafers. The layer thickness was optimized to leave a residual layer after imprinting of thickness ~ 10 nm. Directly after the spin coat cycle the substrate with the liquid sol–gel was loaded in the SCIL tool and the stamp applied in the sol–gel. The sol–gel cross-links as the remaining solvents and reaction products such as water and alcohols are removed from the resist by diffusion into the stamp. After 15 min, the sol–gel solidifies by forming a three-dimensional inorganic network. The stamp was removed from the patterned substrate and a post-cure at 70°C was applied to the sol–gel patterns. The resulting grating patterns are composed of 88 wt% silicon oxide and remaining organic components and are stable in air until 450°C . This provides a stable inorganic etch mask to pattern the underlying GaAs layer.

The residual layer under the imprinted gratings is removed by CF_4 reactive ion etching (RIE) (figure 4(c)(5)). A recipe of 10 sccm CF_4 and 20 sccm nitrogen is used, at a pressure of 12 mT and RF power of 50 W. This results in a linear etch rate of $30\ \text{nm min}^{-1}$ for patterned sol–gel layers. Both gratings were etched for 40 s to remove 20 nm of sol–gel resist and expose the GaAs. This leaves a ~ 80 nm-thick silica etch mask for the 550-nm pitch grating and a ~ 30 -nm thick silica sol–gel mask for the 150-nm pitch grating.

3.3. VCSEL device processing

In order to exclude the effect of variations in the MBE growth, wafers from the same growth run were used and processed into VCSELs. The laser stack is grown on 3" GaAs wafers and consists of a 32-pair DBR (n-type,

GaAs/AlGaAs), a GaAs resonant mode cavity with three GaAs quantum wells between AlGaAs barriers and a 24-pair DBR (p-type, GaAs/AlGaAs) with a 170 nm GaAs layer on top (120 nm spacer, and 50 nm grating height). For single-mode operation current confinement is provided by a high-aluminum content AlGaAs layer placed between the quantum wells and the p-type DBR. This layer is selectively oxidized from the side during processing and provides current and mode confinement [25–27]. Modulated doping was used in the DBRs to reduce optical absorption while maintaining low electrical resistance.

A first batch of samples was patterned with 550-nm pitch gratings by the SCIL sol–gel process and, as a reference, by direct electron-beam patterning of PMMA resist. A second batch was patterned with 550-nm pitch gratings by electron-beam patterning and 150-nm pitch gratings replicated in sol–gel by SCIL. In this manner the quality of the SCIL process can be compared to e-beam fabrication and the performance difference between diffractive and non-diffractive gratings can be measured.

Both batches were processed into single-mode VCSELs using the same processing steps. The first process transfers the sol–gel- or PMMA grating patterns in the GaAs semiconductor using RIE etching with chlorine chemistry. After the GaAs is etched to a target depth of 50 nm, the sol–gel etch mask is selectively removed in aqueous HF and the e-beam resist stripped using organic solvents.

The transfer etch determines the final DBR mirror reflectivity, which is influenced by grating depth and fidelity. Figures 5(a) and (b) show atomic force microscopy (AFM) height data taken perpendicular to the GaAs grating lines after removal of the etch masks. The etch depth in GaAs is 38 nm for the electron-beam-fabricated grating and 58 nm for the grating made using SCIL. This difference is due to the fact that electron-beam polymer resist affects the chlorine etch-chemistry which reduces the etch rate. As both samples were etched for the same time, the resulting depth of the GaAs grating with the sol–gel mask is larger. For the 150 nm grating (figure 5(b)) made using SCIL the target depth of 50 nm is reached. Note that a silica sol–gel etch mask (with a thickness of only 30 nm) is sufficient to etch the GaAs to the target depth, as silica has a high etch selectivity in the chlorine RIE etch. In the AFM data for the 150 nm-pitch grating the corners at the bottom appear rounded. This is due to the finite size of the AFM tip. Figure 5(c) shows a photograph of the wafer with 550-nm pitch gratings in GaAs made by SCIL, clearly showing diffractive colors. The uniform color confirms the wafer-scale pattern transfer—defects in the pattern due to particles, growth defects or wafer bow would otherwise be clearly visible [28].

Figure 5(d) shows a scanning electron microscopy (SEM) image of a finished VCSEL with an imprinted 150-nm pitch grating in the exit aperture. From figure 5 it is clear that the gratings made using SCIL have high fidelity and have identical lateral size control as the patterns made by e-beam lithography.

Next, the wafers were processed into VCSELs using the imprinted alignment markers to align the subsequent layers to the grating areas. The process steps were: RIE mesa etching, lateral oxidation of high Al-containing layer for current and

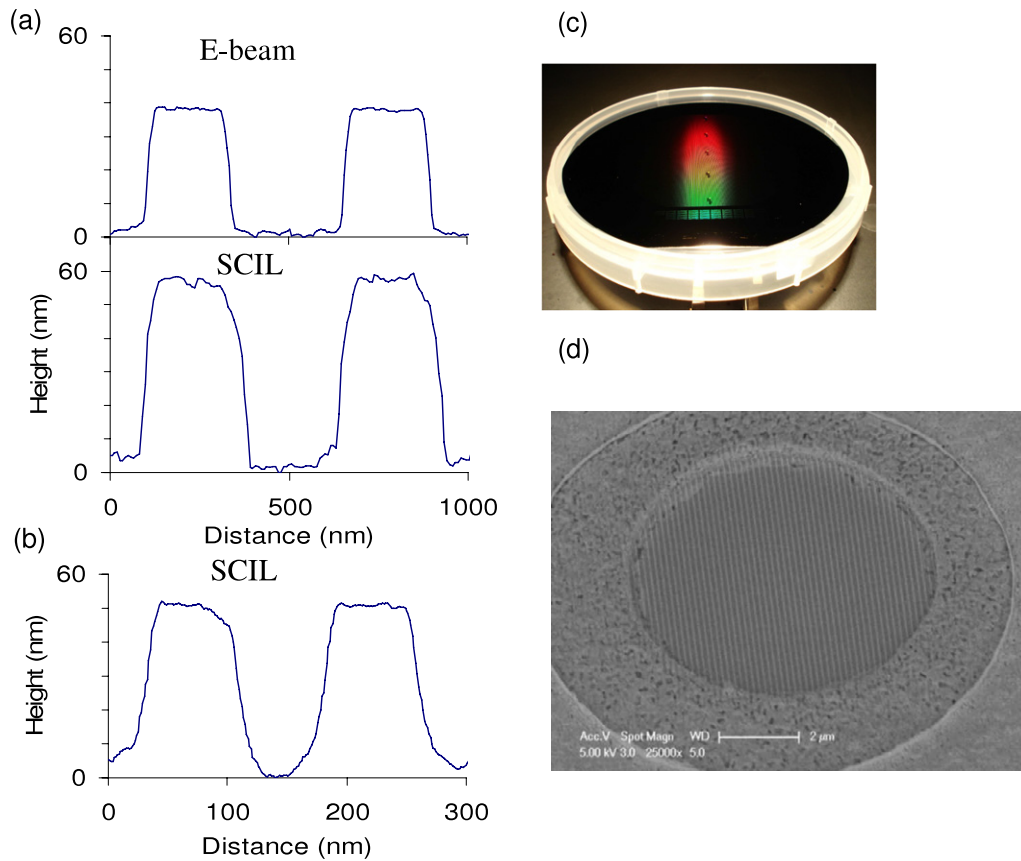


Figure 5. Height profile from AFM measurements of gratings etched in the top GaAs layer of the DBR. (a) Gratings of 550 nm pitch made by electron-beam lithography and SCIL. (b) Grating of 150 nm pitch made by SCIL. (c) Photograph of 3"-diameter GaAs wafer with laser stack with the imprinted and etched 550-nm pitch gratings showing large-area conformality. (d) SEM image taken under 40° of the output aperture of a finished VCSEL with an imprinted 150-nm pitch grating, also showing the surrounding contact metal.

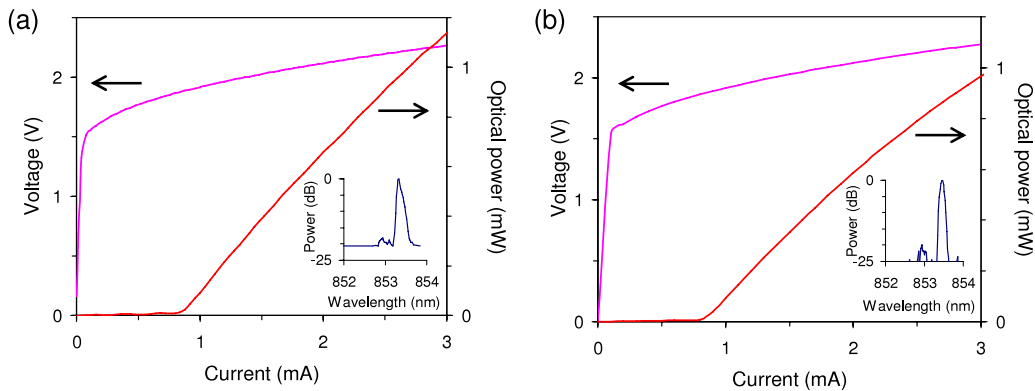


Figure 6. Current–voltage and current–power characteristics for VCSELs with 550-nm pitch gratings fabricated by (a) electron-beam lithography and (b) SCIL. Laser spectra obtained at 2.5 mA driving current are shown as insets.

mode confinement, p- and n-contact formation, polyimide passivation and bond-pad definition. Finally, the wafers were diced into individual VCSEL devices for electrical and optical characterization.

4. VCSEL opto-electronic device characterization

The yield of VCSEL lasers was comparable for the nano-imprint and the e-beam process. All resulting VCSEL devices exhibited single-mode operation. For non-stabilized lasers

the polarization direction is randomly spread over the $\langle 100 \rangle$ and $\langle 010 \rangle$ crystallographic orientations of the GaAs wafer. The laser polarization was measured by positioning a rotating polarizer between the VCSEL and an integrating sphere. All lasers exhibited linear TM polarized lasing and during cycling of the laser current no polarization rotations were measured.

Figure 6 shows current–voltage (*I-V*) and current–power (*I-P*) graphs as well as VCSEL emission spectra measured at a drive current of 2.5 mA for lasers of the first wafer

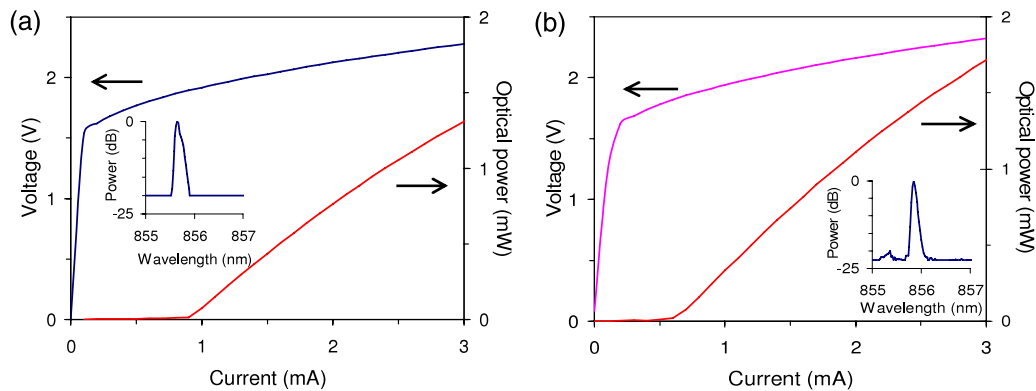


Figure 7. Current–voltage and current–power characteristics for VCSELs with (a) 550-nm pitch gratings fabricated by electron-beam lithography and (b) 150-nm pitch gratings fabricated by SCIL. Laser spectra obtained at 2.5 mA driving current are shown as insets.

batch with 550-nm pitch gratings made by electron-beam lithography (a) and SCIL (b). Both devices have the dominant laser mode emitting at $\lambda = 853.3 \pm 0.1$ nm and are single-mode as can be seen from the side mode suppression ratio of -18 dB and -20 dB for e-beam and SCIL, respectively (see insets). The lasing characteristics of the VCSEL made with an imprinted grating are almost identical to the reference VCSEL which had the grating defined by electron-beam lithography. The I – V and I – P curves are comparable, with a threshold current of 0.84 mA and laser slope of 0.59 mW mA $^{-1}$ (e-beam) and a threshold current of 0.80 mA and laser slope of 0.55 mW mA $^{-1}$ (SCIL), respectively. The optical output power at 3 mA drive current is 1.14 mW (e-beam) and 0.97 mW (SCIL), respectively. The small variation in the I – P behavior between the two samples is attributed to the different etch depths of the gratings (see figure 5). This leads to an increased reflection of the DBR for the SCIL gratings. For the imprinted VCSEL this results in a decreased threshold current and accompanying reduced laser slope. The almost identical opto-electronic behavior of these resonant devices demonstrates that the SCIL imprint method is capable of reproducing deep sub-micron features with the same high fidelity as state-of-the-art electron-beam lithography.

Figure 7 shows I – V and I – P graphs as well as VCSEL emission spectra at 2.5 mA drive current for lasers of the second wafer batch with 550-nm pitch gratings made by e-beam lithography (a) and 150-nm pitch gratings made by SCIL (b). Both devices have the dominant laser mode emitting at $\lambda = 855.7 \pm 0.2$ nm and are single-mode as can be seen from the side mode suppression ratio of -20 dB. From the I – V and I – P graphs it is clear that the performance of VCSELs with a sub-wavelength grating is superior to VCSELs with a diffractive grating. The threshold current is reduced from 0.9 mA for the 550-nm pitch grating laser to 0.6 mA for the 150-nm pitch grating laser. At the same time the laser slope increased from 0.61 mW mA $^{-1}$ for the diffractive grating VCSEL to 0.85 mW mA $^{-1}$ for the sub-wavelength grating VCSEL. This reduction in threshold current and simultaneous increase in laser slope can only be explained by the reduction of losses in the laser cavity as there is no diffraction at the interface of the 150 nm grating. Power in the reflected zeroth order is increased compared to the 550 nm grating

samples which experience diffraction, leading to a reduction in threshold. As the optical losses in the cavity are reduced, the number of emitted photons excited per injected electron increases, leading to an increased laser slope. These data clearly show that using non-diffractive gratings to stabilize the polarization in VCSELs results in a substantially increased efficiency compared to devices with diffractive gratings. The overall efficiency at 3 mA drive current was increased from 19.2% for 550-nm pitch gratings to 24.7% for 150-nm pitch gratings, a relative increase of 29%.

The yield of VCSEL lasers directly after processing of the devices was comparable for devices patterned by electron-beam lithography and SCIL. From the second epitaxial batch we measured the performance of more than 70 000 VCSELs patterned with 550-nm pitch gratings made with e-beam lithography and more than 15 000 VCSELs patterned with 150 nm-pitch gratings made with SCIL. We found that the laser slope efficiency increased from, on average, 0.656 mW mA $^{-1}$ (standard deviation of 0.0349) to a slope efficiency for the 150 nm grating VCSELs of 0.883 mW mA $^{-1}$ (standard deviation of 0.0526), a clear indication that losses in the laser cavity are reduced. We also studied the influence of the SCIL soft nano-imprint process on the lifetime of VCSEL laser devices. Like any semiconductor device, single-mode VCSEL lasers are sensitive to impurities that can diffuse in the semiconductor material and to damage by electrostatic discharge, which can lead to abrupt failure of a VCSEL after a certain time. For lasers made by electron-beam lithography and SCIL (both with 550-nm pitch gratings) an accelerated lifetime test was performed using a 2 mA drive current at a temperature of 140°C . Figure 8 shows the normalized optical output of the same devices, measured at room temperature after 1-day time intervals. The acceleration factor at these conditions is ~ 100 : for these stress tested devices, 10 days corresponds to 3 years of continuous operation under standard conditions. The light output of VCSELs made by SCIL and electron-beam lithography reduces at approximately the same rate for the first few days. For longer times the SCIL laser has a significantly higher power. No abrupt device failures were observed, which indicates that our imprint method does not induce damage to the sensitive semiconductor device during processing.

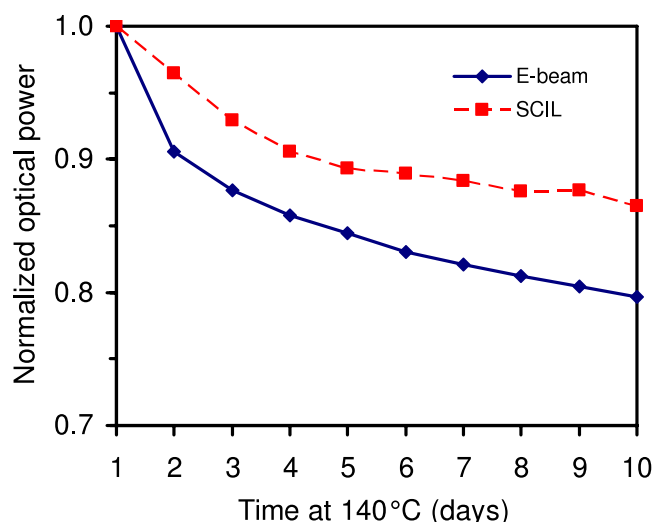


Figure 8. Optical output power of VCSELs with 550-nm pitch gratings made by electron-beam lithography and SCIL as function of time at 140 °C and 2 mA drive current. The optical output power is measured at room temperature at 1-day intervals.

5. Conclusions

Single-mode TM-polarization stabilized GaAs VCSELs operating at $\lambda = 850$ nm have been made by using a soft rubber stamp based nano-imprint method in combination with a sol-gel resist to pattern gratings in the surface mirror. VCSELs prepared by nano-imprinting show equal performance to reference devices produced by electron-beam lithography in terms of emission wavelength, side mode suppression ratio, threshold current, laser slope, output power and lifetime. Imprinted gratings with sub-wavelength pitch do not diffract laser light and VCSEL lasers with these gratings show a reduced threshold current, increased laser slope and increased output power. Overall these VCSEL lasers show a 29% increased efficiency compared to lasers with a conventional diffractive grating. This work demonstrates that the SCIL soft nano-imprint method is capable of delivering nano-scale patterns over wafer-scale areas and enables the fabrication of large-area nano-patterns at high speed and low cost, a key benefit which cannot be delivered by electron-beam lithography.

Acknowledgments

The authors would like to thank colleagues at ULM photonics for VCSEL device processing and characterization and Robert van de Laar of Philips MiPlaza for support on the SCIL imprint process. This work is also part of NANONED, a technology program of the Dutch Ministry of Economic Affairs. This work is also part of the research program of FOM which is financially supported by NWO.

References

- [1] Lackner M, Totschnig G, Loeffler G, Hofbauer H and Winter F 2002 *Therm. Sci.* **6** 13
- [2] Linnerud I, Kaspersen P and Jaeger T 1998 *Appl. Phys. B* **67** 297
- [3] Knappe S, Shah V, Schwindt P D D, Hollberg L, Kitching J, Liew L A and Moreland J 2004 *Appl. Phys. Lett.* **85** 1460
- [4] Lutwak R, Emmons D, Riley W and Garvey R M 2002 *Proc. 34th Annual Precise Time and Time Interval Systems Applications Mtg (Reston, VA, Dec 2002)* p 539
- [5] Ohtoshi T, Kuroda T, Niwa A and Tsuji S 1994 *Appl. Phys. Lett.* **65** 1886
- [6] Tateno K, Ohiso Y, Amano C, Wakatsuki A and Kurokawa T 1997 *Appl. Phys. Lett.* **70** 3395
- [7] Tadanaga O, Tateno K, Uenohara H, Kagawa T and Amano C 2000 *IEEE Photon. Tech. Lett.* **12** 942
- [8] Choquette K D and Leibenguth R E 1994 *IEEE Photon. Technol. Lett.* **6** 40
- [9] Weigl B, Grabherr M, Jung C, Jager R, Reiner G, Michalzik R, Sowada D and Ebeling K J 1997 *IEEE J. Sel. Top. Quantum Electron.* **3** 409
- [10] Dowd P, Heard P J, Nicholson J A, Raddatz L, White I H, Penty R V, Day J C C, Allen G C, Corzine S W and Tan M R T 1997 *Electron. Lett.* **33** 1315
- [11] Debernardi P and Bava G P 2003 *IEEE J. Sel. Top. Quantum Electron.* **9** 905
- [12] Ostermann J M, Debernardi P, Jalics C, Kroner A, Riedl M C and Michalzik R 2005 *Opt. Commun.* **246** 511
- [13] Grabherr M, King R, Jäger R, Wiedenmann D, Gerlach P, Duckeck D and Wimmer C 2008 *Proc. SPIE* **6908** 690803
- [14] Haglund A, Gustavsson J S, Vakusic J A, Jedrasik P and Larsson A 2005 *Electron. Lett.* **41** 805
- [15] Chou S Y, Schablitisky S and Zhuang L 1997 *Proc. SPIE* **3290** 73
- [16] Gustavsson J S, Haglund Å, Vukušić J A, Bengtsson J, Jedrasik P and Larsson A 2005 *Opt. Express* **15** 6626
- [17] Rogers J A, Paul K E and Whitesides G M 1998 *J. Vac. Sci. Technol. B* **16** 88
- [18] Pagliara S, Persano L, Camposeo A, Cingolani R and Pisignano D 2007 *Nanotechnology* **18** 175302
- [19] Moraes C, Sun Y and Simmons C A 2009 *J. Microchem. Microeng.* **19** 065015
- [20] Verschuuren M A and van Sprang H 2007 *Printing Methods for Electronics, Photonics and Biomaterials* vol 1002 (Cambridge: Cambridge University Press and Materials Research Society) p -N03-05
- [21] Aspnes D E, Kelso S M, Logan R A and Bhat R 1986 *J. Appl. Phys.* **60** 754
- [22] Moharam M G and Gaylord T K 1981 *Appl. Opt.* **20** 240
- [23] Jung G Y, Li Z, Wu W, Chen Y, Olynick D L, Wang S Y, Tong W M and Williams R S 2005 *Langmuir* **21** 1158
- [24] Schmid H and Michel B 2000 *Macromolecules* **33** 3042
- [25] Huffaker D L, Lin C C, Shin J and Deppe D G 1995 *Appl. Phys. Lett.* **66** 3096
- [26] Weigl B, Grabherr M, Michalzik R, Reiner G and Ebeling K J 1996 *IEEE Photon. Technol. Lett.* **8** 971
- [27] Grabherr M, Jager R, Michalzik R, Weigl B, Reiner G and Ebeling K J 1997 *IEEE Photon. Technol. Lett.* **9** 1304
- [28] Shift H 2008 *J. Vac. Sci. Technol. B* **26** 458